LARGE-SCALE FORCING MODULATION OF HIGH REYNOLDS NUMBER TURBULENCE IN A VON KÁRMÁN SWIRLING FLOW

Farid Aligolzadeh
Department of Energy and Process Engineering
Norwegian University of Science and Technology
NO-7491 Trondheim, Norway
farid.aligolzadeh@ntnu.no

Pawel Baj
The Faculty of Power and Aeronautical Engineering
Warsaw University of Technology
ul. Nowowiejska 24, 00-665, Warsaw, Poland
pawel.baj@pw.edu.pl

James R. Dawson
Department of Energy and Process Engineering
Norwegian University of Science and Technology
NO-7491 Trondheim, Norway
james.r.dawson@ntnu.no

ABSTRACT

Von Kármán swirling flow is often used as a canonical case to study stationary turbulence experimentally. Although many studies focus on the structure and statistics of turbulence produced at the centre of this flow, several studies focusing on the large-scale global features of the flow have identified interesting phenomena such as equatorial symmetry breaking (de la Torre & Burguete, 2007; Cortet *et al.*, 2010). In this paper, we investigated the potential presence and characteristics of a large-scale slowly rotating structure with high kinetic energy content. The structure was recently identified by Baj *et al.* (2019) at $Re = 3 \times 10^4$. However, we considered a Reynolds number higher than the critical phase transition range proposed by Cortet *et al.* (2010), i.e. $5 \times 10^4 < Re_c < 10^5$. Stereoscopic particle image velocimetry (PIV) was used to measure the stationary flow at $Re = 1.21 \times 10^5$, but such a structure was not observed. However, we found that introducing a modulation with harmonic phase shift between the impellers caused a large-scale oval-shape structure to emerge in the flow. The structure showed oscillations in the axial and circumferential directions of the flow at the modulation frequency, with the axial oscillation being the most significant. The detected structure contained approximately 40% of the kinetic energy of the measured flow.

INTRODUCTION

It is widely agreed that large-scale turbulent motions are flow dependent, whereas their small-scale counterparts possess certain universal features regardless of the flow type. The length scales of the large-scale motions are comparable to the physical size of the flow. Consequently, these motions are greatly impacted by the specific flow geometry, boundary conditions, and instabilities inherent to the flow (Pope, 2000). These motions have been of interest in turbulence research as many natural and engineering applications are related to the large-scale motions, e.g. mixing, drag force, and heat transfer. Some examples of these studies are in pipe flow (Hellström *et al.*, 2015), boundary layer (Lee, 2017), channel flow (Lee *et al.*, 2014), Rayleigh-Bénard flow (Mishra *et al.*, 2011), and Couette flow (Lee & Moser, 2018). The overall conclusion from these studies is that turbulence demonstrates a much wider range of features at large-scales in odds with certain well-established models, e.g. turbulent-viscosity hypothesis. Moreover, large-scale turbulence exhibits nonlocality in time and space, meaning that the turbulent process has a long memory and is influenced by events that occur at remote distances within the flow field (Pope, 2000).

Research on stationary turbulence generated by two counter-rotating discs, known as von Kármán swirling flow, has been conducted since the early works of von Kármán (1921), Batchelor (1951) and Picha & Eckert (1958). The flow is particularly suitable for experimental studies because it produces homogeneous turbulence with high velocity fluctuations and a negligible mean flow at the center of the apparatus, where a stagnation point is established. Most studies on this flow have focused on the dissipation scales near the flow center (Lawson & Dawson, 2015; Debue *et al.*, 2021; Aligolzadeh *et al.*, 2022, 2023). However, the literature on the large-scale features of the flow is relatively limited. de la Torre & Burguete (2007) observed symmetry breaking behavior of the velocity field in a von Kármán flow at $Re \simeq 3 \times 10^5$. This symmetry breaking manifests itself as a slow dynamic, random inversion between two states (bi-stability) when the impellers are counter-rotating. On the other hand, a periodic inversion pattern is observed when a low frequency harmonic forcing is applied to one of the impellers. In a related study, Cortet *et al.* (2010) proposed that turbulence in von Kármán swirling flow undergoes a critical phase transition within the range $5 \times 10^4 < Re < 10^5$. This hypothesis is based on experimental observations of significant maxima required for symmetry breaking within a specific range of impeller forcing. In a recent study, Baj *et al.* (2019) discovered a large-scale, low-frequency velocity structure with high kinetic energy rotating around the axis at $Re \simeq 3 \times 10^4$. The topology of the detected structure reported to be similar to macro-instabilities observed in stirred vessels (Doulgerakis *et al.*, 2011).

The present study aimed to build on the findings of Baj *et al.* (2019) to examine whether the structure exists beyond the critical phase transition Reynolds number reported

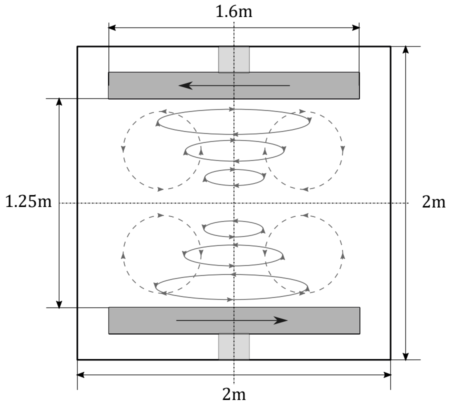

(a)

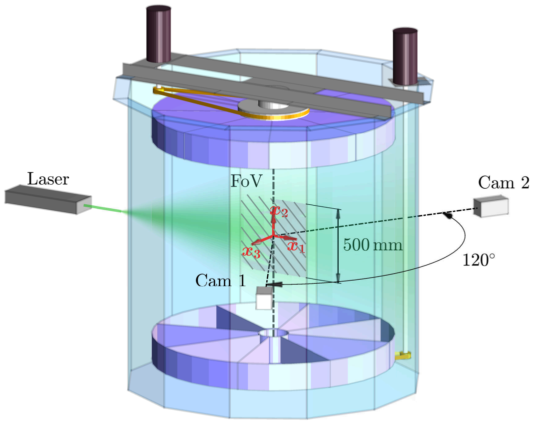

(b)

Figure 1: Von Kármán swirling flow: (a) sketch of the facility along with the key dimensions and the mean flow pattern and (b) the stereoscopic PIV measurement setup.

by Cortet *et al.* (2010). Another objective was to determine whether it was feasible to activate a similar structure by modulating the impellers.

EXPERIMENTAL PROCEDURE

The measurements were conducted in the large-size von Kármán swirling flow facility at Norwegian University of Science and Technology, Trondheim, Norway. Two identical impellers with a radius of $R = 0.8m$ were located at the top and bottom of a dodecagonal transparent plexiglass tank, $2m$ tall and $2m$ across, filled with water. The impellers were $1.25m$ apart. Sub-figure 1a depicts a schematic of the facility, highlighting its key dimensions. Moreover, it illustrates the mean flow pattern, which is characterized by a primary horizontal shear layer. This layer, in turn, induces a secondary vertical circulation pattern due to the centrifugal pumping force.

As a reference case, the two impellers were set to counter-rotate at a speed of 2rpm ($f_0 = 2/60 = 0.033$ Hz, $\Omega_0 = 2\pi f_0$), which corresponded to a Reynolds number of $Re = R^2\Omega_0/\nu \simeq 1.2\times10^5$. In other cases, modulations were introduced either harmonically, as described in equation 1 for the top impeller and equation 2 for the bottom impeller, or randomly using Langevin forcing (see Pope (2000)). In the harmonic cases, modulation amplitude, frequency, and phase shift between the impellers were represented by A_m, f_m, and $\Delta\phi_m$, respectively.

$$\Omega_t(t) = \Omega_0\Big(1 + A_m \sin(2\pi f_m t + \Delta\phi_m)\Big) \tag{1}$$

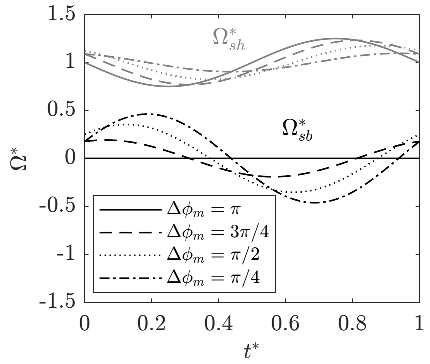

Figure 2: Normalized decomposition of the rotational velocity into shearing, Ω^*_{sh} in gray, and solid body rotation, Ω^*_{sb} in black, in the harmonic modulation cases.

$$\Omega_b(t) = \Omega_0\Big(-1 + A_m \sin(2\pi f_m t)\Big) \tag{2}$$

A total of 11 cases were measured, including the reference case, 8 cases of harmonic modulations, and 2 cases of random modulations. The base case of harmonic modulation was set to $A_m = 0.25$, $f_m/f_0 = 0.1$, and $\Delta\phi_m = \pi$. The rest of the harmonic modulation cases were produced by varying only one of the three parameters in the base case. These parameters took the following values: $A_m = [0.15,\ 0.25,\ 0.35]$, $f_m/f_0 = [0.05,\ 0.1,\ 0.15]$, and $\Delta\phi_m = [\pi/4,\ \pi/2,\ 3\pi/4,\ \pi]$. However, the present paper discusses only the results for $\Delta\phi_m = \pi, 3\pi/4, \pi/2, \pi/4$ while the other two parameters were kept fixed at $A_m = 0.25$ and $f_m/f_0 = 0.1$. Equations 1 and 2 can be used to decompose the normalized rotation speed of the facility into two components: solid body rotation Ω^*_{sb}, i.e. co-rotation, as shown in equation 3, and shearing Ω^*_{sh}, i.e. counter-rotation, as shown in equation 4:

$$\begin{aligned}\Omega^*_{sb}(t) &= \frac{\Omega_t(t)+\Omega_b(t)}{2\Omega_0} \\ &= 2A_m\cos\Big(\frac{\Delta\phi_m}{2}\Big)\sin\Big(2\pi f_m t + \frac{\Delta\phi_m}{2}\Big)\end{aligned} \tag{3}$$

$$\begin{aligned}\Omega^*_{sh}(t) &= \frac{\Omega_t(t)-\Omega_b(t)}{2\Omega_0} \\ &= 1 + A_m\sin\Big(\frac{\Delta\phi_m}{2}\Big)\cos\Big(2\pi f_m t + \frac{\Delta\phi_m}{2}\Big)\end{aligned} \tag{4}$$

When $\Delta\phi_m = \pi$, the two impellers counter-rotate ($\Omega^*_{sb}(t) = 0$). As $\Delta\phi_m$ decreases, amplitude of the harmonic co-rotation between the impellers increases ($\Omega^*_{sb}(t) \neq 0$). The maximum is reached at $\Delta\phi_m = 0$ ($\Omega^*_{sb}(t) = 2A_m\sin(2\pi f_m t)$). In the reference case, only pure shearing was present, i.e. $\Omega^*_{sb,ref}(t) = 0$ and $\Omega^*_{sh,ref}(t) = 1$. Figure 2 demonstrates the profiles of the normalized rotational speed decomposition in different cases over a period of modulation. The correlation coefficient between the solid body and shearing rotations was maximum at $\Delta\phi_m = \pi/2$, with a value of $\rho = 0.01$. It then decreased to $\rho = 0.007$ at $\pi/4$ and $3\pi/4$, and finally reached $\rho = 0$ at $\Delta\phi_m = \pi$.

Stereoscopic PIV was used to measure the velocity fields at the center of the facility. The field of view (FoV) was $\simeq 50\times50\,cm^2$. The spatial resolution of the measurement was

$\Delta x = 3.68\,mm \simeq 13.8\eta$ where η was the Kolmogorov length-scale of the flow. The setup for the stereoscopic PIV measurement is shown in sub-figure 1b. The measurements obtained all three components of velocity in a plane (FoV). To ensure a reasonable convergence of turbulence statistics, the time span of the measurements covered at least 1000 rotations of the impellers based on Ω_0 (2rpm). The length-scales from the measurements were normalized by the impeller radius, $x^* = x/R$, and the time-scales were normalized by the impeller frequency in the reference case, $t^* = t f_0$. Reynolds decomposition was implemented on the velocity fields from the measurements, U_i, to calculate the velocity fluctuations $u_i = U_i - \overline{U_i}$ (Pope, 2000).

RESULTS

To investigate the effect of forcing modulation on the flow field characteristics, the root mean square (rms) of velocity fluctuations and integral length-scales were calculated in different cases followed by power spectral density (PSD) and proper orthogonal decomposition (POD) analyses to provide a more comprehensive picture. Overall, the flow was predominantly affected when $\Delta\phi_m \neq \pi$, i.e. some degree of solid body rotation existed. This can be observed by comparing the results between the cases. The analysis of velocity components indicated that the modulation effect was most pronounced in the axial direction, followed by the circumferential direction, and finally to a limited extent in the radial direction. However, the effect was missing in the flow field when $\Delta\phi_m = \pi$, i.e. pure shearing, even when f_m and A_m were varied.

Table 1 presents the rms of velocity fluctuations averaged over FoV in the modulated cases with different $\Delta\phi_m$ values, normalized by the corresponding values in the reference case. The rms was defined as $u_i' = \langle\overline{u_i^2}\rangle^{1/2}$, where $\overline{*}$ and $\langle * \rangle$ represent ensemble averaging in time (over realizations) and space (over the FoV), respectively. The rms of velocity fluctuations with instantaneous counter-rotation ($\Delta\phi_m = \pi$) was very similar to the reference values. However, by introducing a harmonic phase shift between the impellers, the rms values deviated form the reference case. As the phase shift increased, the rms values in the axial direction exhibited an incremental trend. The maximum value of $\langle u_2' \rangle / \langle u_{2,ref}' \rangle$ was 1.29 at $\Delta\phi_m = \pi/4$. On the other hand, in the radial direction, the rms values decreased as the harmonic phase shift increased. We observe a convex function in the circumferential direction and the total rms, with the minimum values occurring at $\Delta\phi_m = \pi/2$. The convex trend is also observable, to a lesser degree, in the radial and axial directions. Although the authors are uncertain about the reasons behind this behavior, they speculate that the convexity is linked to the forcing strategy. The forcing modulation was the superposition of harmonic shearing and solid body rotation, with the highest correlation at $\pi/2$, as discussed in the experimental procedure section.

To complement the analysis of the velocity fluctuations and investigate whether the changes in kinetic energy are accompanied by changes in the average length-scales of turbulent motions in different directions, the longitudinal integral length-scales in the axial and radial directions of the flow were estimated using equation 5 (De Jong *et al.*, 2009). In this equation, the two point autocorrelation function is calculated over the available range of FoV from a PIV measurement ($0 < r < r_{max}$) followed by fitting an exponential curve to estimate the missing tail outside the measurement domain ($r_{max} < r < \infty$). The measured velocity field in the radial-axial ($x_1 - x_2$) plane was used to calculate L_{11} and L_{22} in table 2.

When the impellers counter-rotated ($\Delta\phi_m = \pi$), the integral length-scales in table 2 varied within $\pm 5\%$ compared to the reference case. However, when solid body rotation was introduced ($0 < \Delta\phi_m < \pi$), a significant continuous growth appeared in the axial direction, accompanied by a decreasing trend in the radial direction. The maximum growth occurred at $\Delta\phi_m = \pi/4$ where $L_{22}/L_{22,ref} = 2.53$. In agreement with this growth in the axial direction, the aspect ratio of the length-scales increased significantly from $L_{22}/L_{11} = 0.68$ in the reference case to $L_{22}/L_{11} = 1.98$ for $\Delta\phi_m = \pi/4$. Thus, modulations with harmonic phase shift between the impellers increased both the kinetic energy and size of the turbulent structure in the axial direction of the flow. The increase in size was more significant than the kinetic energy, i.e. $L_{22}/L_{22,ref} = 2.53$ while $\langle u_2' \rangle / \langle u_{2,ref}' \rangle = 1.29$. This implies that a large-scale motion in the axial direction was activated due to the modulation with some degree of harmonic solid body rotation, where the intensity of this motion varied with $\Delta\phi_m$.

$$L_{ii} = \int_0^{\infty} \frac{\langle \overline{u_i(x) u_i(x + e_i r)} \rangle}{\langle \overline{u_i^2(x)} \rangle} dr \simeq \int_0^{r_{max}} \frac{\langle \overline{u_i(x) u_i(x + e_i r)} \rangle}{\langle \overline{u_i^2(x)} \rangle} dr + \int_{r_{max}}^{\infty} a_i \exp(b_i r)\, dr \tag{5}$$

Table 1: The spatially averaged rms of velocity fluctuations in the radial (u_1'), axial (u_2'), and circumferential (u_3') directions of the flow, normalized by the reference case.

$(A_m, \frac{f_m}{f_0}, \frac{\Delta\phi_m}{\pi})$	$\frac{\langle u_1' \rangle}{\langle u_{1,ref}' \rangle}$	$\frac{\langle u_2' \rangle}{\langle u_{2,ref}' \rangle}$	$\frac{\langle u_3' \rangle}{\langle u_{3,ref}' \rangle}$	$\frac{\langle u' \rangle}{\langle u_{ref}' \rangle}$
(0.25, 0.1, 1)	1.01	1.02	1.00	1.01
(0.25, 0.1, 0.75)	0.98	1.14	1.03	1.03
(0.25, 0.1, 0.5)	0.76	1.13	0.81	0.85
(0.25, 0.1, 0.25)	0.81	1.29	0.97	0.98

Table 2: The longitudinal integral length-scales in the radial (L_{11}) and axial (L_{22}) directions of the flow, normalized by the reference case.

$(A_m, \frac{f_m}{f_0}, \frac{\Delta\phi_m}{\pi})$	$\frac{L_{11}}{L_{11,ref}}$	$\frac{L_{22}}{L_{22,ref}}$	$\frac{L_{22}}{L_{11}}$
(0.25, 0.1, 1)	0.95	1.02	0.74
(0.25, 0.1, 0.75)	0.95	1.30	0.94
(0.25, 0.1, 0.5)	0.91	2.09	1.56
(0.25, 0.1, 0.25)	0.87	2.53	1.98

To further investigate this, figure 3 shows the PSDs of the velocity fluctuations, normalized by the reference case. PSD is defined as the Fourier transform of the auto-correlation function of the velocity fluctuations (equation 6). Figure 3 displays the spatially averaged PSDs of velocity fluctuations in the radial u_1, axial u_2, and circumferential u_3 directions of the flow. The area under the PSD curve in the frequency domain is equal to the rms of the corresponding velocity fluctuation in the real (time) domain. The aim here is to investigate the distribution of kinetic energy in the frequency domain with respect to the reference case. This demonstrates how forcing modulations affected the energy distribution in various directions, and whether energy distribution peaks emerged at certain frequencies.

$$S_{u_iu_i}(f) = \int_{-\infty}^{\infty} R_{u_iu_i}(\tau) e^{-\imath 2\pi f \tau} d\tau \tag{6}$$

Sub-figure 3a, the reference case, does not exhibit any peaks in any direction. The same is observed in sub-figure 3b where $\Delta\phi_m = \pi$. However, sub-figures 3d ($\Delta\phi_m = \pi/2$) and 3e ($\Delta\phi_m = \pi/4$) illustrate significant peaks in the axial and circumferential directions at the modulation frequency $f/f_0 = f_m/f_0 = 0.1$. The peak in the axial direction is more prominent than the circumferential direction. Furthermore, sub-figure 3c ($\Delta\phi_m = 3\pi/4$) exhibits a significant peak in the axial direction at the modulation frequency. However, the peak in the circumferential direction disappears. Figure 3 also indicates that when the peaks emerged, the energy was shifted only from low frequencies toward the peak frequency (modulation frequency) while the higher frequencies remained unaffected, similar to the stationary forcing condition (reference case). This redistribution of kinetic energy in the frequency domain might imply that the signature of large-scale forcing modulation was nearly absent at the smaller scales of the turbulent cascade. Further analysis is required to investigate this in more detail.

To evaluate the characteristic flow motions corresponding to the energy peaks observed in the PSD plots (figure 3), POD analysis was utilized (equation 7):

$$u_i(x_j, t) = \sum_{n=1}^{\infty} a_n(t) \Phi_i^n(x_j) \tag{7}$$

First, we consider the stationary forcing (reference case) and subsequently, the analogous plots for the harmonic forcing modulations are presented. This facilitates the comparison between these cases. Sub-figures 4a and 4b display the first two POD modes ($\Phi_i^n(x_j)$) in the reference case, while sub-figure 4c illustrates the PSDs of the time coefficients of these modes ($PSD(a_n(t))$). No peak appeared in the PSD plots of the coefficients. Finally, sub-figure 4d demonstrates the energy share of the modes, i.e. $(\overline{a_n^2(t)}/\sum_{n=1}^{\infty}\overline{a_n^2(t)}) \times 100(\%))$, indicating that the first four modes accounted for 64% of the total fluctuation energy of the flow, while the first two modes accounted for 47%. Figures 5, 6, 7, and 8 depict plots similar to figure 4, with $\Delta\phi_m$ values of π, $3\pi/4$, $\pi/2$, and $\pi/4$, respectively. The values of $A_m = 0.25$ and $f_m/f_0 = 0.1$ were kept unchanged. In figure 5, when $\Delta\phi_m = \pi$, the PSDs plot did not exhibit any peaks (only the first two are presented here). In figure 6, when $\Delta\phi_m = 3\pi/4$, the PSDs of the first two modes did not show any peaks. However, in modes 3 and 4, peaks appeared at the modulation frequency where the two modes contributed to a total of $12.6 + 6.2 = 18.8\%$ of the kinetic energy of the flow. These modes are topologically paired and together formed a single structure. The PSDs of their time coefficients indicate that this structure oscillated harmonically only in the axial direction at the modulation frequency. However, it was axisymmetric in the circumferential direction without any oscillation

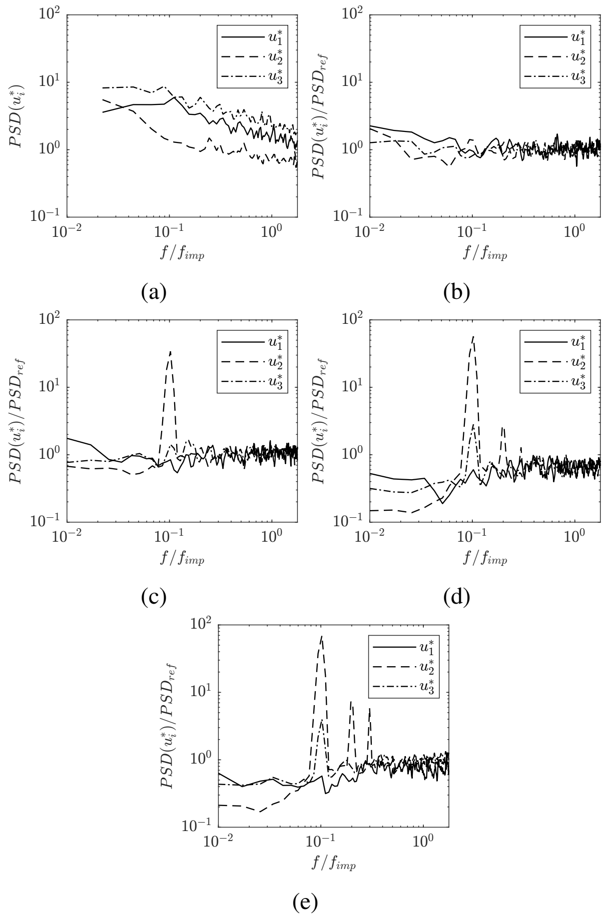

Figure 3: Normalized PSDs of velocity fluctuations in the radial (u_1), axial (u_2), and circumferential (u_3) directions within the cases ($A_m = 0.25$, $f_m/f_0 = 0.1$, $\Delta\phi_m$): (a) reference (no modulation), (b) $\Delta\phi_m = \pi$, (c) $\Delta\phi_m = 3\pi/4$, (d) $\Delta\phi_m = \pi/2$, (e) $\Delta\phi_m = \pi/4$.

at a specific frequency. In figures 7 and 8, PSD peaks appeared in modes 1, 2, and 4 for $\Delta\phi_m = \pi/2$ and $\Delta\phi_m = \pi/4$. The first two modes accounted for $24.3 + 16.1 = 40.4\%$ and $22.8 + 13.6 = 36.4\%$ of the kinetic energy of the flow, respectively. The first two modes are paired and together formed an energetic structure that resembled an oval. In addition, the PSDs of their time coefficients suggest that the structure oscillated harmonically at the modulation frequency in both the axial and circumferential directions.

CONCLUSION

In this paper, we investigated the presence of large-scale harmonic motions in a von Kármán swirling flow at $Re = 1.21 \times 10^5$, a Reynolds number higher than the critical range hypothesised by Cortet *et al.* (2010), i.e. $5 \times 10^4 < Re_c < 10^5$. This study was motivated by the observations of Baj *et al.* (2019) at $Re = 3 \times 10^4$, below the critical range. We used stereoscopic PIV to measure the flow in our large-size facility. No such a structure was detected in the stationary flow. The possibility of activating a similar large-scale harmonically oscillating structure was explored by applying harmonic modulations to the impellers. Various numerical techniques were employed to assess the flow fields from the measurements, such as rms of velocity fluctuations (u_i'), longitudinal integral length-scales (L_{ii}), PSD, and POD. The results indicated that

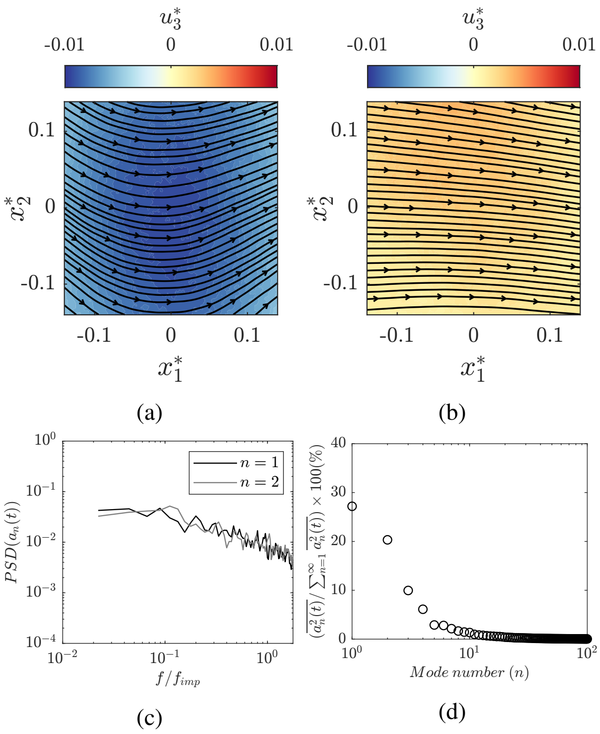

Figure 4: POD analysis of the reference case; (a) mode 1 and (b) mode 2 , i.e. $\Phi_i^{n=1}(x_j)$ and $\Phi_i^{n=2}(x_j)$ where u_1^* and u_2^* are shown as the streamlines and u_3^* as the filled contour. (c) PSDs of the time coefficients of modes 1 and 2. (d) The energy share of the modes.

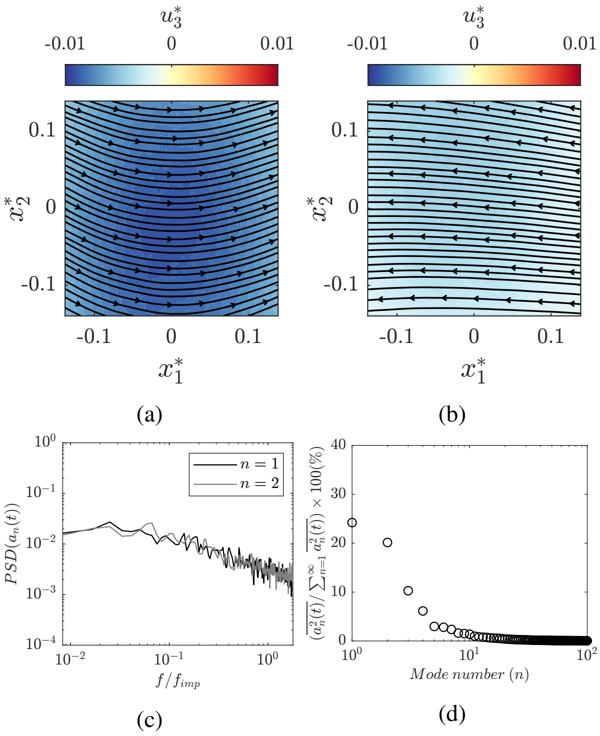

Figure 5: POD analysis of the case ($A_m = 0.25$, $f_m/f_0 = 0.1$, $\Delta\phi_m = \pi$); (a) mode 1 and (b) mode 2 , i.e. $\Phi_i^{n=1}(x_j)$ and $\Phi_i^{n=2}(x_j)$ where u_1^* and u_2^* are shown as the streamlines and u_3^* as the filled contour. (c) PSDs of the time coefficients of modes 1 and 2. (d) The energy share of the modes.

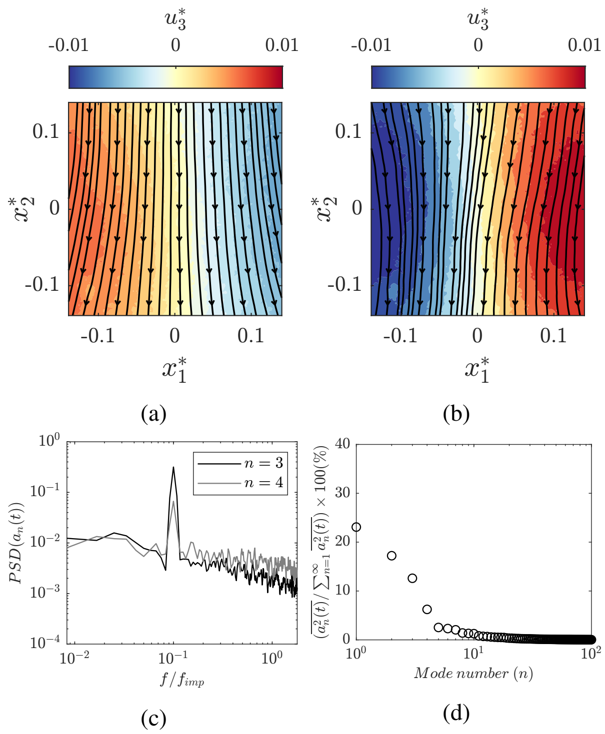

Figure 6: POD analysis of the case ($A_m = 0.25$, $f_m/f_0 = 0.1$, $\Delta\phi_m = 3\pi/4$); (a) mode 3 and (b) mode 4 , i.e. $\Phi_i^{n=3}(x_j)$ and $\Phi_i^{n=4}(x_j)$ where u_1^* and u_2^* are shown as the streamlines and u_3^* as the filled contour. (c) PSDs of the time coefficients of modes 3 and 4. (d) The energy share of the modes.

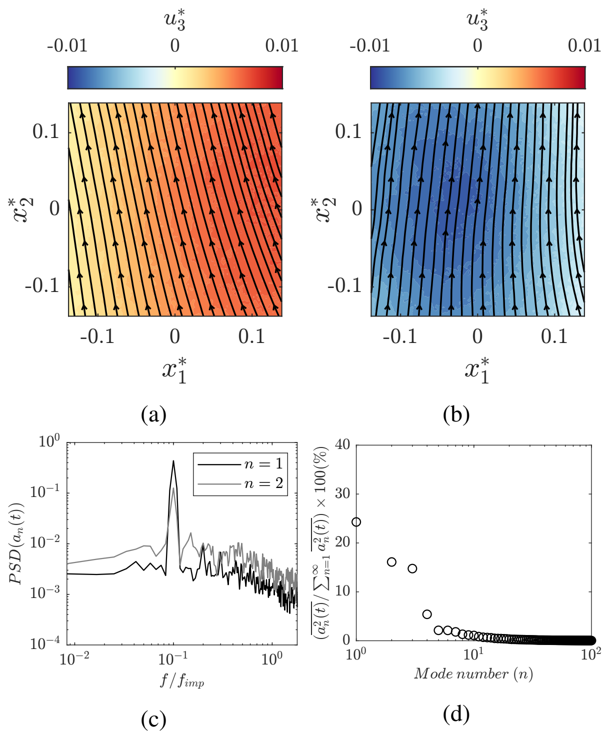

Figure 7: POD analysis of the case ($A_m = 0.25$, $f_m/f_0 = 0.1$, $\Delta\phi_m = \pi/2$); (a) mode 1 and (b) mode 2 , i.e. $\Phi_i^{n=1}(x_j)$ and $\Phi_i^{n=2}(x_j)$ where u_1^* and u_2^* are shown as the streamlines and u_3^* as the filled contour. (c) PSDs of the time coefficients of modes 1 and 2. (d) The energy share of the modes.

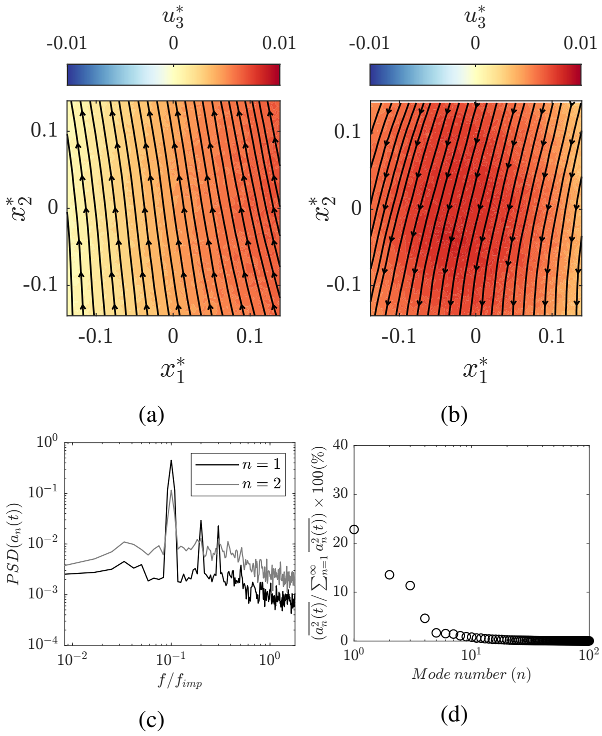

Figure 8: POD analysis of the case ($A_m = 0.25$, $f_m/f_0 = 0.1$, $\Delta\phi_m = \pi/4$); (a) mode 1 and (b) mode 2 , i.e. $\Phi_i^{n=1}(x_j)$ and $\Phi_i^{n=2}(x_j)$ where u_1^* and u_2^* are shown as the streamlines and u_3^* as the filled contour. (c) PSDs of the time coefficients of modes 1 and 2. (d) The energy share of the modes.

when the amplitude of solid body rotation increased (decreasing $\Delta\phi_m$ from π to $\pi/4$), the rms of velocity fluctuations and the longitudinal integral length-scale in the axial direction of the flow, u_2' and L_{22}, showed incremental trends. The growth rate of L_{22} was more pronounced than that of u_2'. The PSD and POD analyses revealed the appearance of a large-scale oval-shape structure in the flow with harmonic oscillations only when solid body rotation was introduced ($\Delta\phi_m \neq \pi$). When $\Delta\phi_m = \pi/4$ and $\pi/2$, the structure showed the most significant energetic harmonic oscillations in the axial direction of the flow, while the circumferential direction showed weaker harmonic oscillations. The oscillating structure accounted for approximately 40% of the kinetic energy of the flow. However, when $\Delta\phi_m = 3\pi/4$, the harmonic oscillation emerged only in the axial direction of the flow, and not in the circumferential direction. This axially oscillating structure accounted for approximately 20% of the kinetic energy of the flow. The radial direction of the flow in the mentioned cases did not exhibit any significant harmonic oscillations.

Acknowledgment

The research leading to these results has received funding from the Norwegian Financial Mechanism 2014-2021 (project no. 2020/37/K/ST8/02594).

REFERENCES

Aligolzadeh, Farid, Holzner, Markus & Dawson, James R. 2022 Study of fine-scale vortical structures in a von kármán mixing flow. In *Proceedings of the 12th International Symposium on Turbulence and Shear Flow Phenomena (TSFP-12)*.

Aligolzadeh, Farid, Holzner, Markus & Dawson, James R 2023 Entrainment, detrainment and enstrophy transport by small-scale vortex structures. *Journal of Fluid Mechanics* **973**, A5.

Baj, Pawel, Dawson, James R., Worth, Nicholas A., Knutsen, Anna N., Lawson, John M. & Bodenschatz, Eberhard 2019 Very large-scale motions in von kármán flow. In *Proceedings of the 11th International Symposium on Turbulence and Shear Flow Phenomena (TSFP-11)*.

Batchelor, Go K 1951 Note on a class of solutions of the navier-stokes equations representing steady rotationally-symmetric flow. *The quarterly journal of mechanics and applied mathematics* **4** (1), 29–41.

Cortet, P-P, Chiffaudel, Arnaud, Daviaud, François & Dubrulle, Bérengère 2010 Experimental evidence of a phase transition in a closed turbulent flow. *Physical review letters* **105** (21), 214501.

De Jong, J, Cao, L, Woodward, SH, Salazar, JPLC, Collins, LR & Meng, H 2009 Dissipation rate estimation from piv in zero-mean isotropic turbulence. *Experiments in fluids* **46**, 499–515.

Debue, P, Valori, V, Cuvier, C, Daviaud, F, Foucaut, J-M, Laval, J-P, Wiertel, C, Padilla, V & Dubrulle, B 2021 Three-dimensional analysis of precursors to non-viscous dissipation in an experimental turbulent flow. *Journal of Fluid Mechanics* **914**, A9.

Doulgerakis, Zacharias, Yianneskis, Michael & Ducci, Andrea 2011 On the manifestation and nature of macroinstabilities in stirred vessels. *AIChE journal* **57** (11), 2941–2954.

Hellström, Leo HO, Ganapathisubramani, Bharathram & Smits, Alexander J 2015 The evolution of large-scale motions in turbulent pipe flow. *Journal of Fluid Mechanics* **779**, 701–715.

von Kármán, Th 1921 Uber laminare und turbulente reibung. *Z. Angew. Math. Mech.* **1**, 233–252.

Lawson, John M & Dawson, James R 2015 On velocity gradient dynamics and turbulent structure. *Journal of Fluid Mechanics* **780**, 60–98.

Lee, Jin, Lee, Jae Hwa, Choi, Jung-Il & Sung, Hyung Jin 2014 Spatial organization of large-and very-large-scale motions in a turbulent channel flow. *Journal of fluid mechanics* **749**, 818–840.

Lee, Jae Hwa 2017 Large-scale motions in turbulent boundary layers subjected to adverse pressure gradients. *Journal of Fluid Mechanics* **810**, 323–361.

Lee, Myoungkyu & Moser, Robert D 2018 Extreme-scale motions in turbulent plane couette flows. *Journal of Fluid Mechanics* **842**, 128–145.

Mishra, Pankaj Kumar, De, Arnab K, Verma, Mahendra K & Eswaran, Vinayak 2011 Dynamics of reorientations and reversals of large-scale flow in rayleigh–bénard convection. *Journal of fluid mechanics* **668**, 480–499.

Picha, KG & Eckert, ERG 1958 Study of the air flow between coaxial disks rotating with arbitrary velocities in an open or enclosed space. *proceedings of 3rd US Nat. Cong. Appl. Mech* .

Pope, Stephen B 2000 *Turbulent flows*. Cambridge university press.

de la Torre, Alberto & Burguete, Javier 2007 Slow dynamics in a turbulent von kármán swirling flow. *Physical review letters* **99** (5), 054101.